Numerical analysis of heat conduction problems on 3D general-shaped domains by means of a RBF Collocation Meshless Method

IOP Conf. Series: Journal of Physics: Conf. Series **923** (2017) 012034 doi:10.1088/1742-6596/923/1/012034

Numerical analysis of heat conduction problems on 3D general-shaped domains by means of a RBF Collocation Meshless Method

R Zamolo[1] and E Nobile[1]

[1] Dipartimento di Ingegneria e Architettura, Università degli Studi di Trieste, via A. Valerio 10, 34127 Trieste, Italy

E-mail: riccardo.zamolo@phd.units.it

Abstract. A Collocation Meshless Method based on Radial Basis Function (RBF) interpolation is employed to solve steady state heat conduction problems on 3D domains of arbitrary shape. The set of points required by the numerical method is generated through a novel and simple technique which automatically produces a distribution with variable point density and which adapts to each specific geometry. Numerical results are systematically compared to the corresponding analytical solutions considering several combinations of parameters; convergence tests have also been carried out. The favorable properties that will be outlined suggest that this approach can be an effective and flexible tool in the numerical simulation of heat conduction problems with complex 3D geometries.

Keywords:
Meshless methods, Local RBF, 3D node/point generation, Octree, Poisson equation

1. Introduction

The simulation of engineering relevant problems with standard numerical approaches (Finite Element and Finite Volume methods among all) requires a spatial discretization of the domain; such phase, known as meshing, can require a valuable fraction of the entire simulation time, especially when dealing with complex 3D geometries.

In recent years, several *meshless* approaches have been proposed [1–5] to avoid the need of a mesh: only a set of points is required to approximate the unknown physical quantities and the field equations, with slight constraints on the distribution of points; these approaches have been successfully applied to a wide range of problems, from heat transfer to solid mechanics.

Meshless methods employing Radial Basis Function (RBF) interpolation [6–11] will be considered; in particular, Hardy's Multiquadric (MQ) [12] can be used as RBF; such MQ-RBF meshless approaches are becoming more and more popular in the field of numerical simulations because of their efficiency, accuracy and flexibility [13–16].

The original MQ-RBF method [13, 14] employed a global support for the RBF interpolation, which leads to spectral convergence and insensitivity to point locations, at the price of dealing with fully populated matrices [16]; this approach becomes clearly unfeasible as the number of unknowns N grows, because of excessive time and memory consumptions. Futhermore the choice of interpolation parameters had strong influence on the numerical results.

Instead of a globally supported interpolation, most of recent MQ-RBF meshless approaches [17–21] use a local support for the RBF interpolation, which allows the use of efficient solvers at the price of a loss of spectral convergence and greater sensitivity to point locations; for these reasons a locally supported strategy will be employed in this work.

MQ-RBF meshless methods require a distribution of points which covers the whole domain and its boundary; higher point density is required where the solution exhibit large gradients because of the local support, as in a traditional mesh-based method, but without any other constraint on the distribution. In this work the point distributions will be generated by a novel and simple technique which is based on an Octree space partitioning algorithm [22] to obtain a variable point density which mets a defined spacing function; then a refinement process is employed to adapt the distribution to the domain boundaries. This refinement process also smooths the local spacing discontinuities due to the Octree algorithm.

Several computations will be carried out considering two 3D geometries and various combinations of parameters for a *Poisson* equation (steady state heat conduction) in order to outline the properties of this numerical approach; computed solutions will be compared to the corresponding analytical solutions and FEM solutions. These tests showed that this approach can be an accurate and flexible tool in the numerical simulation of heat conduction problems on complex-shaped 3D domains.

2. Governing equation and boundary conditions

Let us consider the following 3D Poisson equation in the unknown temperature field T:

$$-\nabla^2 T = q \tag{1}$$

defined on the domain Ω; equation (1) is representative of steady state heat conduction problems with internal heat generation q, in the case of a constant $k = 1$ thermal conductivity.

Two different kinds of boundary conditions (BC) will be considered; *Dirichlet* BC (prescribed temperature) on the Dirichlet boundary Γ_D:

$$T = \bar{T} \tag{2}$$

and *Neumann* BC (prescribed heat flux) on the Neumann boundary Γ_N:

$$\frac{\partial T}{\partial \mathbf{n}} = \mathbf{n} \cdot \nabla T = \bar{f} \tag{3}$$

where $\mathbf{n}$ is the exterior normal to the boundary $\Gamma = \partial\Omega$; obviously we have $\Gamma_D \cup \Gamma_N = \Gamma$.

Since the computed solution will be compared to the corresponding analytical solution T_{an}, we will set $\bar{T} = T_{an}$ and $\bar{f} = \mathbf{n} \cdot \nabla T_{an}$; the domain Ω and the terms q and T_{an} will be defined case by case.

3. Point distributions

A point distribution is defined as a set of N points $\mathbf{x}_i \in \Omega$ whose local spacing is weakly defined as the mean distance from $\mathbf{x}_i$ to its nearest neighbors.

The point distribution process is composed by two consecutive phases:

- Octree phase: an Octree algorithm is used to generate a distribution of points whose local spacing is close to a prescribed spacing function $\bar{s}(\mathbf{x})$; starting from the smallest box bounding Ω, the algorithm recursively partitions the space in 8 octants till the local partitioned box, centered in $\mathbf{x}_i$, has a size $l \leq \bar{s}(\mathbf{x}_i)$: this point is then inserted if $\mathbf{x}_i \in \Omega$;

- Refinement phase: since the Octree algorithm produces a distribution inside Ω but not on its boundary Γ, a simple point refinement process is employed to move the points near Γ onto it; this is accomplished moving the points according to the reciprocal repulsion of points: each point is subjected to the radial repulsion force of the closest 14 points.
  The repulsion force magnitude is chosen to be the following:

$$F(r) = \omega \bar{s} \left[4 \left(\frac{r}{\bar{s}} \right)^2 + 1 \right]^{-2} \tag{4}$$

  where r is the distance between the points and $\omega = 0.5$ is a relaxation parameter.
  This refinement phase is iterated 30 times over the whole point set, and whenever the distance from a point $\mathbf{x}_i$ to the boundary is less than the local spacing $\bar{s}(\mathbf{x}_i)$, the point is projected onto Γ; 30 iterations are typically enough to obtain a boundary distribution whose local spacing is comparable to $\bar{s}$ (there are no "holes" or clustered patches on the boundary). The refinement phase also smooths the local spacing discontinuities inside Ω due to the Octree algorithm.

4. Numerical method

4.1. Local RBF interpolation

RBF interpolation approximates the field T around $\mathbf{x}$ through the following expansion [9]:

$$T(\mathbf{x}) = \sum_{j \in J_n(\mathbf{x})} a_j \varphi(\|\mathbf{x} - \mathbf{x}_j\|) + \mathbf{b} \cdot \mathbf{x} + c \tag{5}$$

where $J_n(\mathbf{x})$ represents the indices j of the n points $\mathbf{x}_j$ closest to $\mathbf{x}$ in the usual Euclidean norm. $T(\mathbf{x})$ is therefore a linear combination of n radial functions φ centered at the n field points $\mathbf{x}_j$ plus a linear polynomial in $\mathbf{x}$.

There are many possible choices for φ [10]; Hardy's Multiquadric (MQ) has been chosen since it seems to offer the better results if an appropriate *shape factor* ε is employed [15, 16]:

$$\varphi(r) = \sqrt{1 + (\varepsilon r)^2} \tag{6}$$

The coefficients a_j, $\mathbf{b}$ and c can be formally computed writing equation (5) for the $m \leq n$ closest points $\mathbf{x}_i$, $i \in J_n(\mathbf{x})$ which do not lie on the Neumann boundary Γ_N:

$$T(\mathbf{x}_i) = T_i \tag{7}$$

where T_i is the unknown temperature in $\mathbf{x}_i$.

The following additional relations are needed [3] because of the linear polynomial in (5):

$$\sum_{j=1}^{n} a_j = 0 \quad , \quad \sum_{j=1}^{n} x_j a_j = 0 \quad , \quad \sum_{j=1}^{n} y_j a_j = 0 \quad , \quad \sum_{j=1}^{n} z_j a_j = 0 \tag{8}$$

If any of the neighbor points $\mathbf{x}_i$, $i \in J_n(\mathbf{x})$ lies on the Neumann boundary, for each of these $n - m$ Neumann points the corresponding BC (3) must be satisfied:

$$\mathbf{n} \cdot \nabla T(\mathbf{x}_i) = \bar{f}_i \tag{9}$$

where $\nabla T(\cdot)$ is given by the gradient of equation (5) with $\nabla \varphi(r_j) = \varepsilon^2 \mathbf{r}_j / \varphi(r_j)$, $\mathbf{r}_j = \mathbf{x} - \mathbf{x}_j$.

Collecting the n coefficients a_i, the m unknown values T_i and the $n - m$ Neumann boundary contributions $\bar{f}_i$ in column vectors $\mathbf{a}$, $\mathbf{T}$ and $\bar{\mathbf{f}}$, respectively, the interpolation system, in compact form, is the following:

$$\mathbf{G}\begin{Bmatrix}\mathbf{a}\\ \mathbf{b}\\ c\end{Bmatrix}=\begin{Bmatrix}\mathbf{T}\\ \mathbf{0}\\ \bar{\mathbf{f}}\end{Bmatrix} \tag{10}$$

4.2. Rescaled Multiquadrics

For each local MQ-RBF interpolation, the shape parameter has been rescaled as $\varepsilon = \bar{s}_{max}\bar{\varepsilon}/d_k$ to avoid ill-conditioned interpolation matrices where the prescribed spacing function $\bar{s}$ is small; $\bar{\varepsilon}$ is the modified shape parameter (called shape parameter from now on), $\bar{s}_{max}$ is the maximum spacing within the domain and d_k is the local subdomain size, defined as the maximum distance between the points $\mathbf{x}_i$, $i \in J_n(\mathbf{x_k})$ near $\mathbf{x_k}$.

4.3. Collocation

Equation (1) with RBF approximation (5) becomes:

$$\nabla^2 T(\mathbf{x}) = \sum_{j\in J_n(\mathbf{x})} a_j \nabla^2 \varphi(\|\mathbf{x}-\mathbf{x}_j\|) = -q(\mathbf{x}) \tag{11}$$

where the 3D Laplacian of the RBF φ is $\nabla^2\varphi(r_j) = [2\varphi(r_j) + 1/\varphi(r_j)][\varepsilon/\varphi(r_j)]^2$, $r_j = \|\mathbf{x}-\mathbf{x}_j\|$.

Writing equation (11) for a generic point $\mathbf{x}_k$ near $\mathbf{x}$ gives:

$$\mathbf{a}^T\mathbf{L}(\mathbf{x}_k) = -q(\mathbf{x}_k) \tag{12}$$

where $\mathbf{L}(\mathbf{x}_k)$ is the column vector of the Laplacian of the RBF φ evaluated in $\mathbf{x}_k$ for each of the n neighbors $\mathbf{x}_j$. Finally, recalling $\mathbf{a}^T$ from equation (10) we have:

$$\left\{\begin{array}{cccc}\mathbf{T}^T & \mathbf{0} & \bar{\mathbf{f}}^T\end{array}\right\}[\mathbf{G}^T]_a^{-1}\mathbf{L}(\mathbf{x}_k) = -q(\mathbf{x}_k) \tag{13}$$

where $[\mathbf{G}^T]_a^{-1}$ is the left $(n+4)\times n$ submatrix of $[\mathbf{G}^T]^{-1}$. Writing equation (13) for each point $\mathbf{x}_k$ which does not lie on the boundary gives the following linear system:

$$\mathbf{A}_{II}\mathbf{T}_I = -(\mathbf{q} + \mathbf{A}_{ID}\mathbf{T}_D + \bar{\mathbf{f}}_N) \tag{14}$$

where the subscripts I, D, and N refer to *Internal*, *Dirichlet* and *Neumann* contributions, respectively; since $\mathbf{A}_{II}$ is nonsymmetric, sparse and very large, an iterative solver has to be used. The biconjugate gradient stabilized method (BiCGSTAB) [23] with diagonal preconditioning has been employed with a relative tolerance of 1E-8, which converged in less than 150 iterations for each case that has been considered.

4.4. Error norm and FEM results

The comparison between the computed solution T_{comp} and the corresponding analytical solution T_{an} will be done computing the normalized root-mean-square norm of the error (NRMSE):

$$\text{NRMSE} = \sqrt{\frac{1}{V(\Omega)}\int_\Omega \left(\frac{T_{comp}-T_{an}}{T_{max}-T_{min}}\right)^2 d\Omega} \tag{15}$$

where $V(\Omega)$ is the volume of Ω; the 3D integral has been approximated by numerical quadrature using the prescribed spacing function $\bar{s}^3$ as quadrature weight.

Finite Element results have been obtained using COMSOL Multiphysics® FEA software using tetrahedral meshes with linear elements (4 nodes); the number of mesh nodes is kept closest possible to the number of unknowns N of the corresponding meshless solution, as well as the element sizing which is chosen to be closest possible to the prescribed spacing function $\bar{s}(\mathbf{x})$. Dirichlet BC have been prescribed, while different BC had negligible influences on the error.

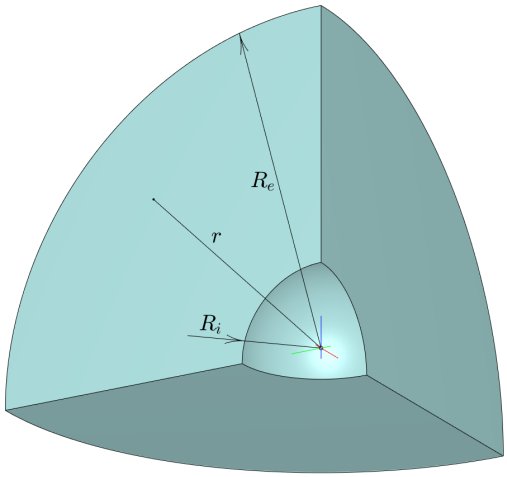

Figure 1. Test case A: geometry.

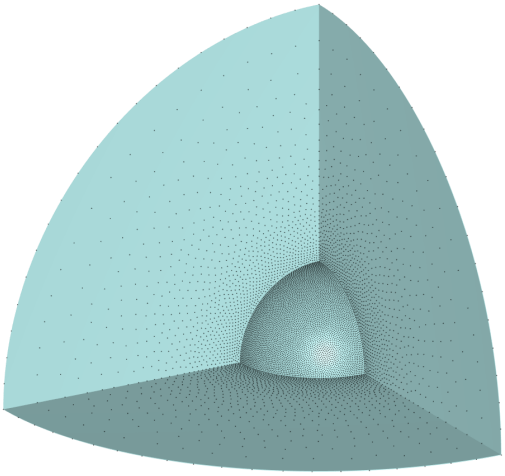

Figure 2. Test case A: boundary point distribution with $N \approx 40$k points.

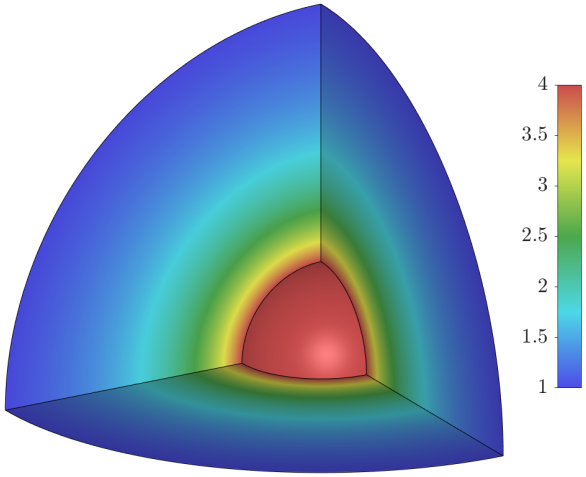

Figure 3. Test case A: surface plot of the solution.

5. Numerical results and discussion

5.1. Test case A: 1/8 of a spherical shell

The geometry of the problem is reported in Figure 1 where the center of the spherical shell is also the origin for the spherical r coordinate; the ratio R_i/R_e is chosen to be 0.25.

The chosen analytical solution is the following:

$$T_{an} = R_e/r \tag{16}$$

which is harmonic: $q = -\nabla^2 T_{an} = 0$; the prescribed spacing function is chosen to be $\bar{s} \propto r^2$. A surface plot of this solution is reported in Figure 3, while a boundary point distribution for $N \approx 40$k points can be seen in Figure 2.

Boundary conditions

- A1: Dirichlet BC on the whole boundary;

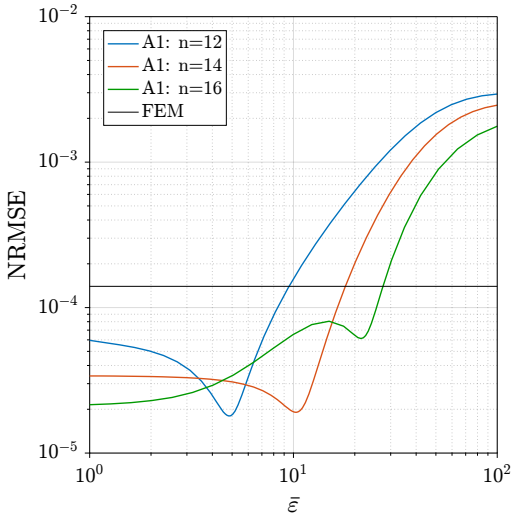

Figure 4. Test case A1: error vs shape parameter with Dirichlet BC, $N \approx 100$k.

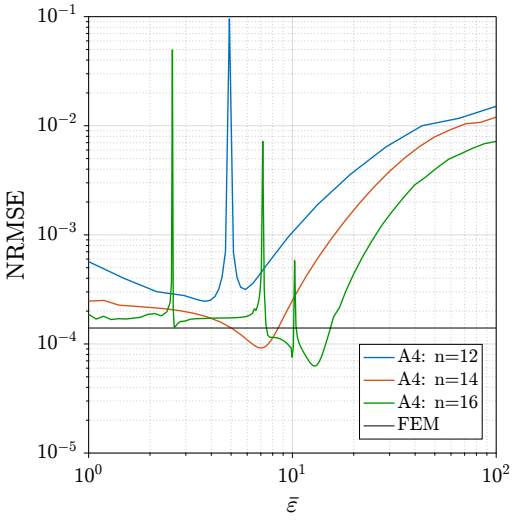

Figure 5. Test case A4: error vs shape parameter with Mixed BC, $N \approx 100$k.

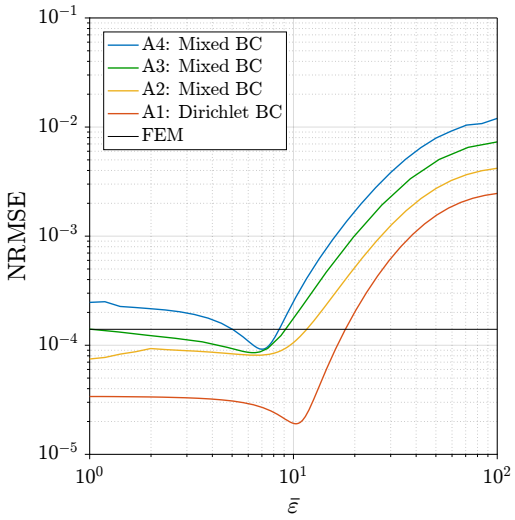

Figure 6. Test case A: error vs shape parameter with $n = 14$, $N \approx 100$k.

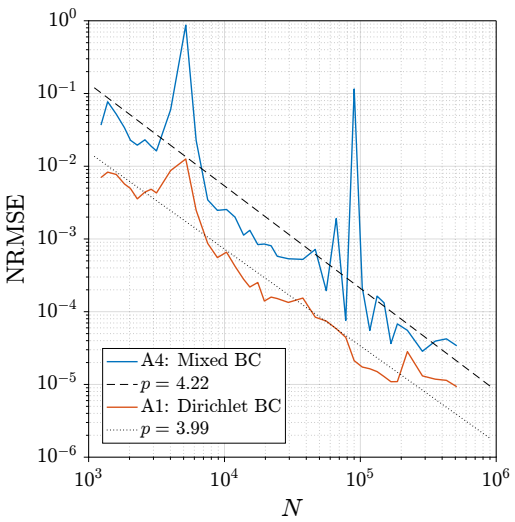

Figure 7. Test case A: convergence curves with $n = 12$ and $\bar{\varepsilon} = 5$.

- A2: Neumann BC on one flat face, Dirichlet BC elsewhere;
- A3: Neumann BC on two flat faces, Dirichlet BC elsewhere;
- A4: Neumann BC on three flat faces, Dirichlet BC elsewhere.

First of all we investigated the influence of the shape parameter $\bar{\varepsilon}$ in the range $[1, 100]$ on the error, considering three cases with n=12, 14 and 16 local interpolation points and two different BC, A1 and A4, Figures 4 and 5, with $N \approx 100$k points. These figures show that with Dirichlet BC, for each n there exists a value of the shape parameter which minimizes the error; for $n = 16$ the error has a local minimum which is not global in the considered range. For all the values of n, there exists a value of $\bar{\varepsilon}$ below which the error is lower than the FEM. With Mixed BC, Figure

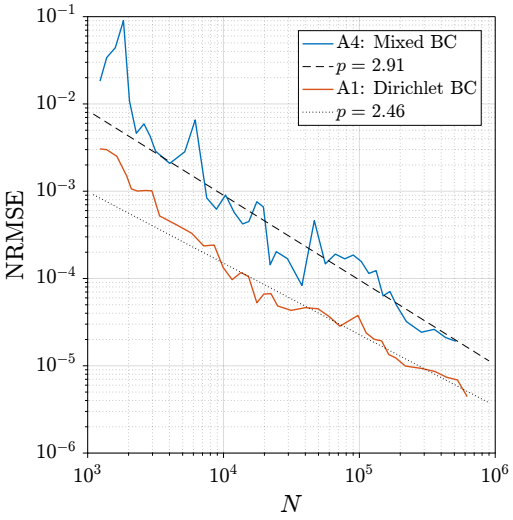

Figure 8. Test case A: convergence curves with $n = 14$ and $\bar{\varepsilon} = 5$.

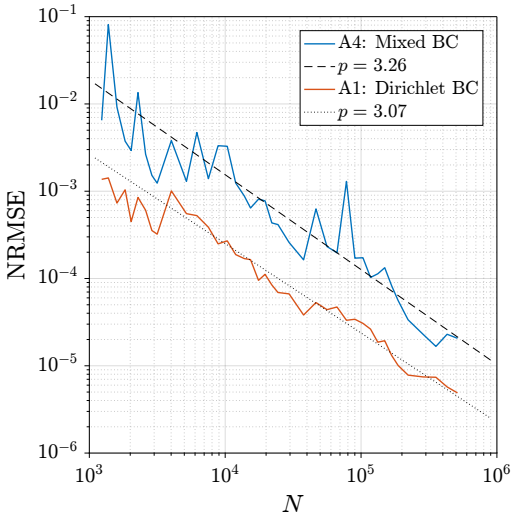

Figure 9. Test case A: convergence curves with $n = 16$ and $\bar{\varepsilon} = 5$.

5, an irregular and peaked behaviour is observed, except for the $n = 14$ case; this undesired feature is therefore due to the imposition of Neumann BC on a portion of the boundary: further analyses have to be carried out in order to understand the influence of local point distribution and shape factor when dealing with Neumann BC within the local MQ-RBF interpolation. In addition to this irregular behaviour, the errors are comparable with FEM only for small ranges of $\bar{\varepsilon}$ around 10.

Figure 6 shows the influence of $\bar{\varepsilon}$ on the error for all the considered BC with $n = 14$ and $N \approx 100$k points: a behaviour with minimum error around $\bar{\varepsilon} = 10$ is visible for all the curves, with growing error passing from Dirichlet BC (A1) to Mixed BC (A4); the errors for this case with $n = 14$ are comparable with the FEM for a wide range of $\bar{\varepsilon}$ and for each BC.

Figures 7-9 show convergence curves for three cases with n=12, 14 and 16 local interpolation points with $\bar{\varepsilon} = 5$. We first note that for every n there is a difference of one order of magnitude in the error passing from Dirichlet BC (A1) to Mixed BC (A4), while the irregular behaviour of the curves is probably due to the nature of the point distribution process (Octree phase) which has discontinuous dependence from the prescribed spacing function $\bar{s}$. In particular the case $n = 12$ presents strong discontinuities, while the cases $n = 14$ and $n = 16$ have a similar and more regular behaviour with estimated order of accuracy[1] p varying from 2.5 to 3.3.

5.2. Test case B: hemisphere with cylindrical through hole

The geometry of the problem is reported in Figure 10 where r is the distance from the vertical axis and z starts from the center of the hemisphere; the ratio R_i/R_e is chosen to be 0.5.

The chosen analytical solution is the following:

$$T_{an} = \exp\left(k_z\left(\frac{z}{H} - 1\right)\right) \exp\left(k_r \frac{R_i - r}{R_e - R_i}\right) \tag{17}$$

with $k_z = 1.5$ and $k_r = 1.0$; T_{an} has therefore exponential growth in the direction of the upper circular edge located at $z = H = \sqrt{R_e^2 - R_i^2}$, as can be seen in the surface plot of Figure 12.

[1] For 3D cases the order of accuracy p is defined by: NRMSE $\sim N^{-p/3}$.

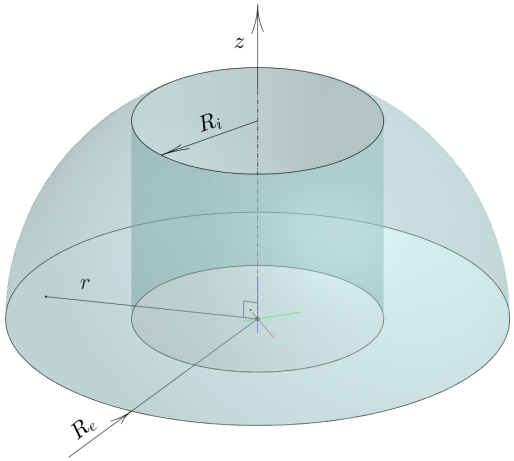

Figure 10. Test case B: geometry.

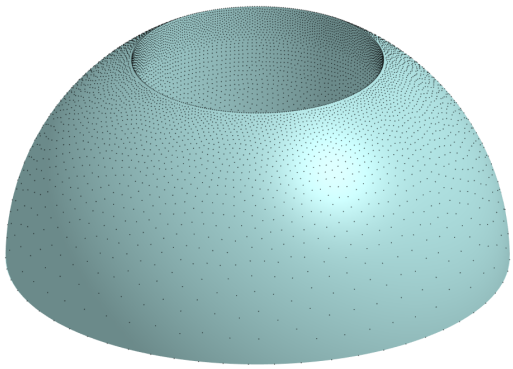

Figure 11. Test case B: boundary point distribution with $N \approx 50$k points.

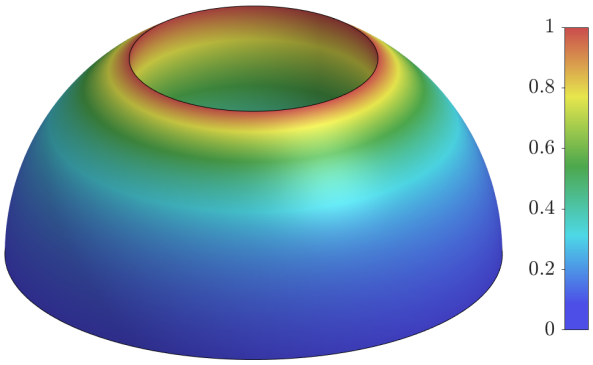

Figure 12. Test case B: surface plot of the solution.

The prescribed spacing function is chosen to be $\bar{s} \propto T_{an}^{-1}$: a boundary point distribution for $N \approx 50$k points can be observed in Figure 11.

The internal heat generation q is therefore:

$$q = -\nabla^2 T_{an} = -\big[(C_z^2 + C_r^2) + C_r/r\big]T_{an} \tag{18}$$

where $C_z = k_z/H$ and $C_r = -k_r/(R_e - R_i)$.

Boundary conditions

- B1: Dirichlet BC on the whole boundary;
- B2: Neumann BC on the spherical surface, Dirichlet BC elsewhere.

Again, we first investigated the influence of the shape parameter $\bar{\varepsilon}$ in the range $[1, 100]$ on the error, considering three cases with n=12, 14 and 16 local interpolation points and two different BC, B1 and B2, Figures 13 and 14, with $N \approx 100$k points. Dirichlet BC error curves have very similar behaviour for different n, with no local minimal points in the considered range for $\bar{\varepsilon}$; below $\bar{\varepsilon} = 10$ the error is lower than the FEM, even one order of magnitude less than FEM error for $\bar{\varepsilon}$ around 1. With Mixed BC, Figure 14, the error curves have shifted towards large errors,

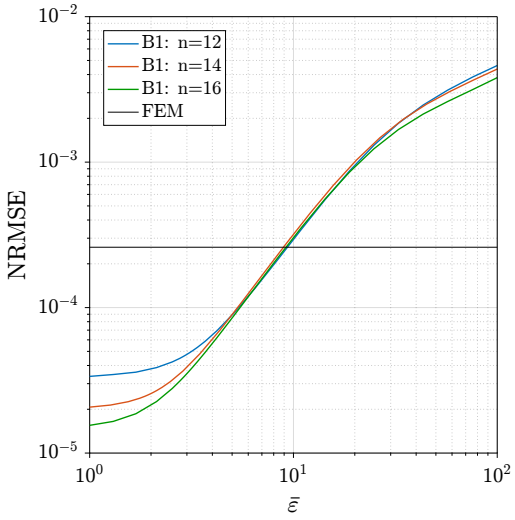

Figure 13. Test case B1: error vs shape parameter with Dirichlet BC, $N \approx 100$k.

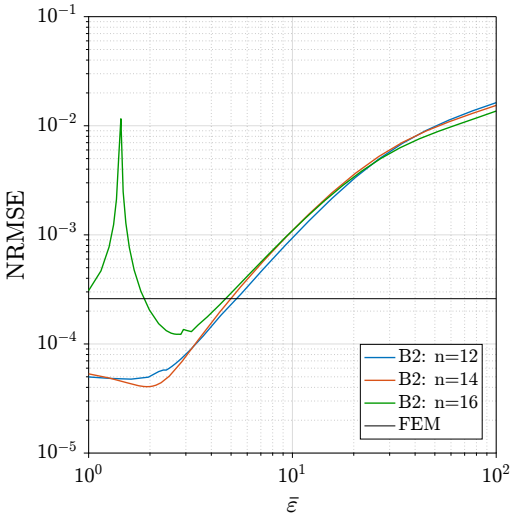

Figure 14. Test case B2: error vs shape parameter with Mixed BC, $N \approx 100$k.

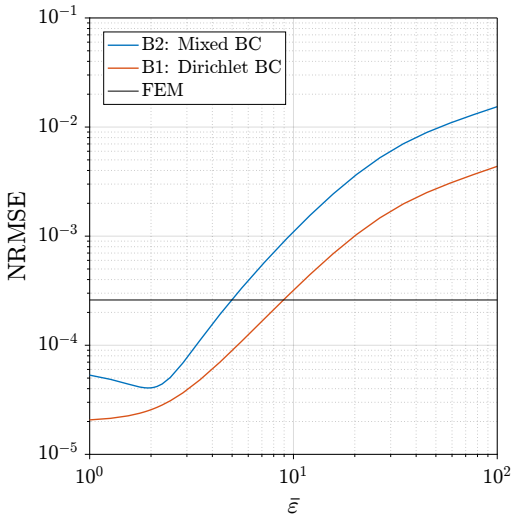

Figure 15. Test case B: error vs shape parameter with $n = 14$, $N \approx 100$k.

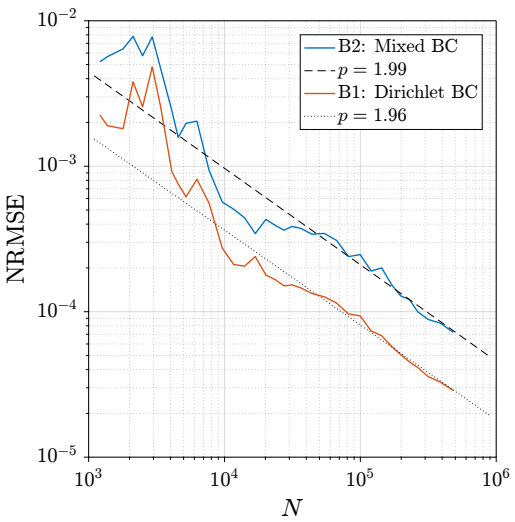

Figure 16. Test case B: convergence curves with $n = 12$ and $\bar{\varepsilon} = 5$.

while a peak is observed for the $n = 16$ case around $\bar{\varepsilon} = 1.3$; for $n = 12$ and 14 the errors are lower than FEM only for $\bar{\varepsilon} < 5$.

Figure 15 shows the influence of $\bar{\varepsilon}$ on the error for both Dirichlet and Mixed BC with $n = 14$ and $N \approx 100$k points: a decreasingly error for small $\bar{\varepsilon}$ is visible for both curves, with growing error passing from Dirichlet BC (B1) to Mixed BC (B2); the errors for this case $n = 14$ are comparable to the FEM for a wide range of $\bar{\varepsilon}$ and for both BC.

Figures 16-18 show convergence curves for three cases with n=12, 14 and 16 local interpolation points with $\bar{\varepsilon} = 5$. Again we note that for every n there is a difference of a factor 5 in the error passing from Dirichlet BC (B1) to Mixed BC (B2), while the irregular behaviour of the curves is less evident than the test case A. Furthermore for large N the convergence curves become more

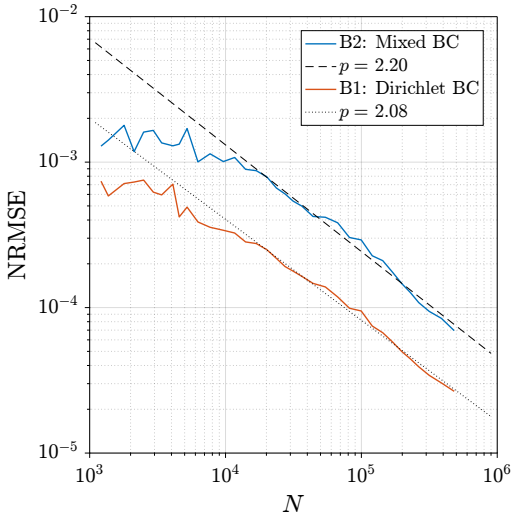

Figure 17. Test case B: convergence curves with $n = 14$ and $\bar{\varepsilon} = 5$.

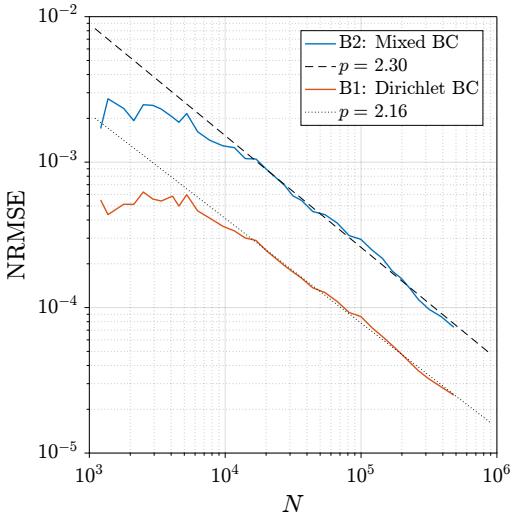

Figure 18. Test case B: convergence curves with $n = 16$ and $\bar{\varepsilon} = 5$.

and more regular, allowing an estimation of the order of accuracy p between 2.0 and 2.3.

5.3. CPU times

Among all phases of the proposed approach, the point distribution process is the most time consuming; its cost is approximately 1 second/50k points[2] and its complexity is linear in N. The local interpolation phase has a cost which is the half of the previous phase, approximately 1 second/100k points in the case of $n = 14$ and is again linear in N; the solution phase through BiCGSTAB algorithm took the same amount of time of the local interpolation phase for N around 500k and $n = 14$. We remark that the point distribution process and the local interpolation phase are not parallelized in any way, while BiCGSTAB is automatically parallelized on multicore architectures within MATLAB®.

6. Conclusions and future work

In this work a Collocation Meshless Method, based on Multiquadric Radial Basis Function interpolation, is used for the numerical simulation of steady state heat conduction problems (Poisson equation) on complex-shaped 3D domains. A simple and flexible process is employed to generate a distribution of points with a prescribed spacing; points are automatically generated inside the domain and on its boundary.

Two test cases of practical relevance have been considered, and for each case several computations are carried out for various combinations of parameters (total number of points N, shape factor $\bar{\varepsilon}$, number of local interpolation points n, boundary conditions). Most of these tests revealed good accuracy (comparable with linear FEM) and good convergence properties (more than second order in space); excellent results are obtained with $n = 14$ (the asymptotic number of edges per node in a tetrahedral mesh with recursive baricentric partitioning is exactly 13 [24], corresponding to the choice $n = 14$).

These positive results confirm that the coupling of the local RBF meshless discretization with the point generation process here presented can therefore be extremely effective in the numerical simulation of heat conduction problems on general-shaped 3D domains of engineering relevance.

[2] On a modern laptop (quad-core Intel® i7 2.6GHz).

Further investigations will be conducted considering a variable number of local interpolation points n and a variable shape factor $\bar{\varepsilon}$, different strategies for shape factor rescalation and improved point distribution techniques.

References

[1] Liu G 2003 *Meshfree Methods: Moving Beyond the Finite Element Method* (CRC Press) ISBN 978-1-4200-8209-8
[2] Li H and Mulay S 2013 *Meshless Methods and Their Numerical Properties* (CRC Press) ISBN 978-1-4665-1747-9
[3] Fasshauer G 2007 *Meshfree Approximation Methods with MATLAB* (World Scientific) ISBN 978-981-270-633-1
[4] Belytschko T, Krongauz Y, Organ D, Fleming M and Krysl P 1996 *COMPUT METHOD APPL M* **139**(1–4) 3–47
[5] Nguyen V, Rabczuk T, Bordas S and Duflot M 2008 *MATH COMPUT SIMULAT* **79**(3) 763–813
[6] Franke C and Schaback R 1998 *APPL MATH COMPUT* **93**(1) 73–82
[7] Fasshauer G 1997 *In: Surface Fitting and Multiresolution Methods* ed Mehaute A L, Rabut C and Schumaker L (Vanderbilt University Press) pp 131–138
[8] Zerroukat M, Power H and Chen C 1998 *INT J NUMER METH ENG* **42**(7) 1263–1278
[9] Golberg M, Chen C and Bowman H 1999 *ENG ANAL BOUND ELEM* **23**(4) 285–296
[10] Larsson E and Fornberg B 2003 *COMPUT MATH APPL* **46**(5–6) 891–902
[11] Fornberg B and Flyer N 2015 *ACTA NUMER* **24** 215–258
[12] Hardy R 1971 *J GEOPHYS RES* **76**(8) 1905–1915
[13] Kansa E 1990 *COMPUT MATH APPL* **19**(8-9) 127–145
[14] Kansa E 1990 *COMPUT MATH APPL* **19**(8-9) 147–161
[15] Franke R 1982 *MATH COMPUT* **38**(157) 181–200
[16] Sarra S and Kansa E 2009 *Multiquadric Radial Basis Function Approximation Methods for the Numerical Solution of Partial Differential Equations* (*Advances in Computational Mechanics* vol 2) ed Atluri S N (Tech Science Press)
[17] Šarler B 2007 *From Global to Local Radial Basis Function Collocation Method for Transport Phenomena* vol 5 (Springer) chap 14, pp 257–282
[18] Šarler B and Vertnik R 2006 *COMPUT MATH APPL* **51**(8) 1269–1282
[19] Mavric B and Šarler B 2015 *INT J NUMER METHOD H* **25**(6) 1488–1510
[20] Wang Z, Huang Z, Zhang W and Xi G 2015 *NUMER HEAT TR B-FUND* **67**(4) 320–337
[21] Waters J and Pepper D 2015 *NUMER HEAT TR B-FUND* **68**(3) 185–203
[22] Aluru S 2004 *Quadtrees and Octrees* (Chapman and Hall/CRC) chap 19, pp 19/1–19/26
[23] der Vorst H A V 1992 *SIAM J SCI STAT COMP* **13**(2) 631–644
[24] Plaza A and Rivara M 2002 *J COMPUT APPL MATH* **140**(1-2) 673–693